Deprotonation and Cation Adsorption on the NiOOH/Water Interface: A Grand-Canonical First-Principles Investigation

Mohammad J. Eslamibidgoli[a], Jun Huang[a,b], Piotr M. Kowalski[a], Michael H. Eikerling[a,c], Axel Groß[b,d,*]

[a] *Institute of Energy and Climate Research, Theory and Computation of Energy Materials (IEK-13), Forschungszentrum Jülich, 52425 Jülich, Germany*
[b] *Institute of Theoretical Chemistry, Ulm University, Albert-Einstein-Allee 11, D-89069 Ulm, Germany*
[c] *Chair of Theory and Computation of Energy Materials, Faculty of Georesources and Materials Engineering, RWTH Aachen University, Aachen 52062, Germany*
[d] *Helmholtz Institute Ulm (HIU), Electrochemical Energy Storage, 89069, Ulm, Germany*

Abstract

Nickel-based oxides are highly active, cost effective materials for the oxygen evolution reaction in alkaline conditions. Recent experimental studies have revealed the importance of surface deprotonation and alkali metal cation adsorption on the activity of Ni oxide surfaces, in contact with aqueous alkaline electrolyte. As a first step to elucidate the role of the alkali adsorption for the activity, we performed first-principles electronic structure calculations to address the stable surface structures of β-NiOOH(0001) as a function of the operating conditions in an electrochemical environment. We present a grand-canonical approach to compute the surface Pourbaix diagram of the β-NiOOH/water interface for the processes of deprotonation and alkali metal cation adsorption. The results of this study emphasize the importance of double layer effects, including the adsorbate-induced change of surface dipole moments and the rearrangement of water molecules due to their strong interaction with the adsorbed species, for the most stable interface structure.

Keywords: Nickel (Oxy)hydroxides; Deprotonation; Pourbaix Diagram;

*Corresponding author
Email address: axel.gross@uni-ulm.de (Axel Groß)

Oxygen Evolution; Density Functional Theory; Computational Hydrogen Electrode

1. Introduction

Green hydrogen will be essential as a fuel of a defossilized energy economy [1]. Compared with conventional fuels such as coal, natural gas and oil, hydrogen has the highest specific energy [2], and if used in fuel cells it constitutes a clean, efficient and sustainable technology [3].

An already well-developed and cost-effective green technology for hydrogen production is alkaline water electrolysis, in which hydrogen gas is produced from the water splitting reaction under alkaline conditions [4]. In alkaline electrolyzers the anode and the cathode are immersed in highly concentrated alkaline solutions (e.g., NaOH or KOH). These electrodes are separated by a porous and electrically insulating separator material, which is filled with a highly ionically conducting medium for hydroxide ions (OH^-) transport from cathode to anode. The separator hinders H_2 and O_2 gases to crossover between the electrodes.

The electrochemical oxidation and reduction reactions take place at the anode and cathode surface, respectively. At the anode, the oxygen evolution reaction (OER: $4OH^- \rightarrow 2H_2O + O_2 + 4e^-$) produces oxygen gas, O_2, while at the cathode, hydrogen gas is produced via reduction of water in the hydrogen evolution reaction (HER: $4H_2O + 4e^- \rightarrow 2H_2 + 4OH^-$) [4]. The standard equilibrium potential of the overall water splitting reaction is 1.23 V. However, the practical operating cell voltage for hydrogen evolution lies between 1.5-2.0 V. The additional voltage, also referred to as overvoltage or overpotential, must be applied to overcome the energy barriers of the OER. The overall system efficiency thus remains between 59-70 % for commercially available electrolysers [5, 6]. Improvement of this efficiency and increasing the hydrogen production rate are pivotal practical goals to achieve for this technology.

Ni-based oxides are earth-abundant materials and recognized as promising electrocatalyst materials for alkaline electrolysers. They offer a favourable combi-

nation of high electrochemical activity and stability [7, 8]. Many attempts have been made to improve the electrochemical activity of Ni materials via modification of the composition and structure of the catalyst material, e.g., using doping it with iron [9, 10]; via novel synthetic design of nanoparticles and porous materials to increase the active surface area [11, 12, 13, 14]; or OER enhancement through modifications in pH or the type and concentration of ionic species in the electrolyte [15, 16].

Recent experimental studies by Diaz-Morales *et al.* and Garcia *et al.* have revealed the importance of surface deprotonation as well as alkali metal cation adsorption on the OER activity of nickel oxyhydroxide (NiOOH) surfaces in contact with the alkaline electrolyte [15, 16]. The earlier study by Diaz-Morales *et al.* employed *in situ* Surface Enhanced Raman Spectroscopy (SERS) to investigate pH-dependent interfacial changes of NiOOH under OER conditions [15]. It was found that in highly alkaline pH, the degree of surface deprotonation increases, thereby producing negatively charged surface species ($NiOO^-$) that lead to an enhanced OER activity [15].

Garcia *et al.*. investigated the effect of electrolyte alkali metal cations (A^+, where A is Li, Na, K, Cs) on OER activity of NiOOH. The consistent activity trend of $Cs^+ > Na^+ > K^+ > Li^+$ was found for both pure NiOOH as well as NiOOH containing iron impurities. Combining the deprotonation and alkali metal cation adsorption effects, one may speculate that the interaction of cations with negatively charged surface oxygen species (NiOO-A^+) plays an important role in stabilizing cations on the surface [16].

Even more recently, the mechanism of OER based on deprotonation was investigated on the (0001) facet of NiOOH using density functional theory (DFT), which provided further support for the role of deprotonation in OER activity [17]. These calculations suggested that the deprotonation step is the potential-determining step with an overpotential of 0.44 V. It was discussed that this step also oxidizes Ni^{3+} to Ni^{4+}, while not changing the oxidation state of surface oxygen atoms [17].

As a prerequisite for understanding the kinetic processes involved in the OER,

the relevant local reaction conditions at the interface need to be revealed. Any mechanistic study should be preceded by the identification of the stable adsorbate structures [18]. Herein, we employ a first-principles grand-canonical approach to explore the thermodynamic stability of NiOOH/water interfaces for the processes of deprotonation and alkali metal cation adsorption under varying electrochemical conditions with respect to pH and electrode potential. We will discuss the crucial importance of double-layer effects such as the adsorbate-induced surface dipole moment as well as the explicit presence of water molecules [19, 20, 21, 22] for the computed surface Pourbaix diagrams.

2. Computational Methods

Model system. The bulk structure of β-NiOOH used in our simulations is based on our previous study [23]. It is represented as a model system with a $1 \times 2 \times 1$ unit cell, the stability of which compares well with the most stable bulk phases reported in the literature [24]. The material has the ABBCC oxygen stacking sequence [25], for which hydrogen atoms present in the inter-layer space create a saturated number of hydrogen bonds between the layers, in agreement with infrared spectroscopy measurements [26]. Surface structures were modelled as three-layer slabs of β-NiOOH(0001) with 3×4 unit cells. Stoichiometric surface structures include 12 Ni atoms, 24 O atoms, as well as 12 H atoms per layer of the slab for β-NiOOH(0001). These unit cell configurations are commensurate with the addition of explicit water layers. A water coverage of 5/6 ML at NiOOH(0001), initially equilibrated with *ab initio* molecular dynamics simulation at 140 K for 8 ps (1 fs time-step), was used [23]. The H-down configuration of water was found to be more stable on NiOOH(0001) due to formation of H-bonds between water and unsaturated surface O atoms.

The (0001) facet of NiOOH is terminated with 50% of O* and 50% OH*, as shown in Fig. 1 (a). Surface deprotonation was modelled by successive removal of surface H atoms from the surface, while keeping the unit cell electroneutral at any given degree of deprotonation. Thereafter, adsorption of Li^+, Na^+, K^+ and

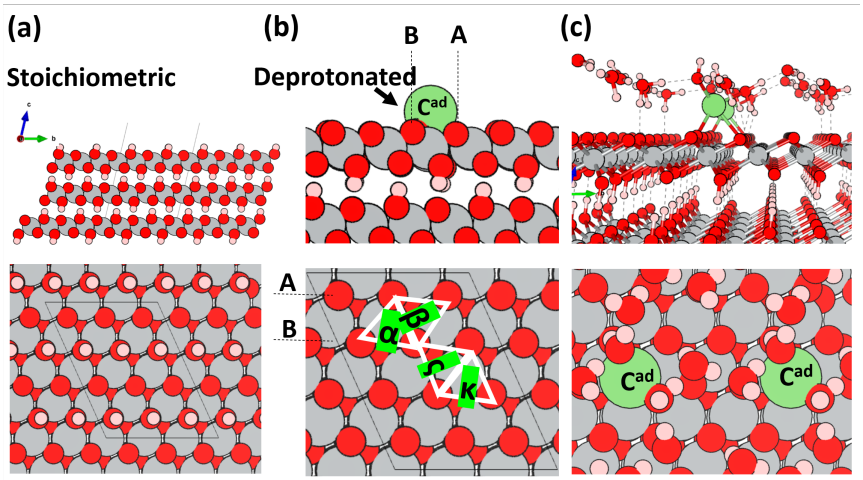

Figure 1: Side and top views of the stoichiometric NiOOH(0001) slab considered in this study. Gray, red and pink are Ni, O and H atoms, respectively. (a) Shows the stoichiometric system. (b) Side and top views of fully-deprotonated NiOOH(0001), indicating the four possible three-fold adsorption sites, among which site α was found to be the most stable for alkali metal cations. The green atom represents an adsorbed cation. (c) Side and top views of the fully deprotonated cation adsorbed surface covered with explicit water molecules

Cs^+ ions on the fully deprotonated surface was considered, as shown in Fig. 1 (b). To find the most stable adsorption site for cations, all possible surface O adsorption sites on the deprotonated surface - including all atop, bridge and the three-fold sites - were examined, from which the cations were found to be stabilized only on the four possible three-fold sites. Among these sites, site α, as shown in Fig. 1 (b), was found to be the most stable site for all cations, which is on top of the surface Ni atom and involves two of the deprotonated O atoms, as shown in Fig. 1 (b). The relative stability of these four sites is provided in Tab. 1.

DFT+U calculations. Spin-polarized DFT-based calculations were performed with the Vienna Ab initio Simulation Package (VASP) [27, 28]. The ionic cores were represented by projector augmented waves (PAW) [29]. Kohn–Sham one-electron wave functions were expanded in a plane wave basis set with an

Table 1: Relative stability of cation adsorption on various adsorption sites at deprotonated NiOOH(0001) (see Fig. 1)

Adsorption site	Li (meV)	Na (meV)	K (meV)	Cs (meV)
α	0.0	0.0	0.0	0.0
β	61.3	63.9	62.5	56.2
κ	181.0	193.0	75.6	54.4
ζ	158.0	174.0	51.8	46.9

energy cutoff of 500 eV. Electronic exchange and correlation effects were incorporated within the generalized gradient approximation (GGA), using the PBE exchange–correlation functional [30]. The DFT+U method has been employed to account for the strong correlations of *d*-electrons of Ni atoms. We used the approach by Dudarev *et al.* [31] with an effective Hubbard U_{eff} parameter (U–J) of 5.5 eV, which was calculated by Li and Selloni [32] using linear response theory [33]. A geometry relaxation for bulk NiOOH was performed with a $12\times12\times8$ Monkhorst–Pack k-point mesh [34] and a force threshold of 0.01 eV Å^{-1}. For geometry optimizations of the slab models, we used $5 \times 5 \times 1$ k-points, and a force threshold of 0.05 eV Å^{-1}.

Grand-canonical approach. Our goal is to explore the thermodynamic stability of the NiOOH(0001)/water system for the processes of deprotonation and cation adsorption under varying electrode potential and pH. This can be achieved by employing the combination of periodic DFT calculations and the grand-canonical approach based on the computational hydrogen electrode (CHE) [35, 36, 37, 38]. In this approach, the change in the Gibbs free energy due to the formation of interface structure, normalized by the unit area, is given by,

$$\Delta\gamma = \frac{1}{A}\left(\Delta\ \mathrm{G}_{ads}^{tot} - \sum_i\ n_i\mu_i\right), \tag{1}$$

where, $\Delta\mathrm{G}_{ads}^{tot}$ is the change in the Gibbs free energy of adsorption, μ_i is the electrochemical potential of ions in the electrolyte, and n_i is the number of

Table 2: Standard redox potentials and cohesive energies of alkali metals

Cation	half-cell reaction	U^0 (V vs. SHE)	$E_A^{cohesive}$ (eV)
Li^+	$Li^+(aq) + e^- \rightleftharpoons Li(s)$	$U^0 = -3.04$	-1.63
Na^+	$Na^+(aq) + e^- \rightleftharpoons Na(s)$	$U^0 = -2.714$	-1.113
K^+	$K^+(aq) + e^- \rightleftharpoons K(s)$	$U^0 = -2.925$	-0.934
Cs^+	$Cs^+(aq) + e^- \rightleftharpoons Cs(s)$	$U^0 = -3.03$	-0.804

adsorbed species i per unit cell surface area, A. In the CHE scheme, it is assumed that the electrode and the electrolyte are thermodynamic reservoirs for electrons and ions such as protons, respectively, whereas the reference system typically corresponds to the standard hydrogen electrode (SHE) [35, 39]. At standard conditions (T=298 K, and P= 1 atm, and pH = 0), molecular hydrogen in the gas phase is in equilibrium with the solvated proton and the electron ($\frac{1}{2}H_2\,(g) \rightleftharpoons H^+(aq) + e^-$). Therefore, in thermodynamic equilibrium the corresponding chemical potential of hydrogen in the gas phase is equal to that of a proton-electron pair. Consequently, referring the potential to the SHE, we can avoid the calculation of the proton solvation energy in water and instead use the gas-phase energy of H_2 which can easily be calculated based on DFT:

$$\widetilde{\mu}_{H^+} + \widetilde{\mu}_{e^-} = \frac{1}{2}\mu_{H_2} - eU_{\mathrm{SHE}} - k_B T \ln(10)\,\mathrm{pH}. \tag{2}$$

This way, the adsorption free energy is approximated by the total binding energy obtained using periodic DFT calculations, while the electrode potential U and pH enter this equilibrium expression to account for deviations from the standard conditions. The CHE is not only applicable to coupled proton-electron transfer processes but it can also be applied to any solvated ionic species [35, 40, 41]. For alkali metal cations A^+, this can be realized by the half-cell reaction, $A^+\,(aq) + e^- \rightleftharpoons A\,(s)$ at $U = U^0$ vs. SHE, where U^0 corresponds to the standard redox potential, as listed in Tab. 2.

In thermodynamic equilibrium,

$$\widetilde{\mu}_{\mathrm{A}^+} + \widetilde{\mu}_{e^-} = \mu_{\mathrm{A}} - e\left(U_{\mathrm{SHE}} - U^0\right) + k_{\mathrm{B}}T\ln\left(a_{\mathrm{A}^+}\right), \tag{3}$$

where $a_{\mathrm{A}^+}$is the thermodynamic activity of the cation A^+. We assumed an activity of 0.1, which for an ideal solution correspond to a cation concentration of 0.1 M. The derivation of the Gibbs free energy of adsorption for the independent processes of deprotonation and cation adsorption is provided in the Supplementary Information (SI). For both processes of deprotonation and alkali metal cation adsorption at NiOOH(0001)/water, the total free energy is given by,

$$\Delta\gamma^{total} = \frac{1}{A}\left(\Delta\ \mathrm{E}^{tot}_{ads} - n_{\mathrm{H}}\Delta\widetilde{\mu}_{\mathrm{OH}^-} - \ n_C\Delta\widetilde{\mu}_{\mathrm{A}^+}\right), \tag{4}$$

where $\Delta\mathrm{G}^{tot}_{ads}$ can be approximated by $\Delta\mathrm{E}^{tot}_{ads}$, which is obtained from DFT calculations, neglecting entropy and zero-point energy corrections, n_H is the number of hydrogen atoms removed from the surface and n_{A} is the number of adsorbed cations. Moreover, we have

$$\Delta E^{tot}_{ads} = E_{slab-ads|(water)} - E_{slab|(water)} + \frac{n_{\mathrm{H}}}{2}E_{\mathrm{H}_2} - n_{\mathrm{A}}E^{cohesive}_{\mathrm{A}}, \tag{5}$$

with

$$\Delta\widetilde{\mu}_{\mathrm{OH}^-} = \ eU_{\mathrm{SHE}} + k_{\mathrm{B}}T\ln\left(10\right)\mathrm{pH}, \tag{6}$$

and

$$\Delta\widetilde{\mu}_{\mathrm{A}^+} = -e\left(U_{\mathrm{SHE}} - U^0\right) + k_{\mathrm{B}}T\ln(a_{\mathrm{A}^+}). \tag{7}$$

In Eq. 5, $E^{cohesive}_{\mathrm{A}}$ is the cohesive energy of alkali metals, the values of which are shown in Tab. 2. $E_{slab-ads|(water)}$ and $E_{slab|(water)}$ are the total energies of the optimized slab (including a water layer) with and without adsorbed species, calculated from DFT.

Equation 4 can be expressed as an equation of two-dimensional planes for the different surface configurations and a specified cation activity as a function of electrode potential and pH. This is shown in Fig. 2 for the case of deprotonation

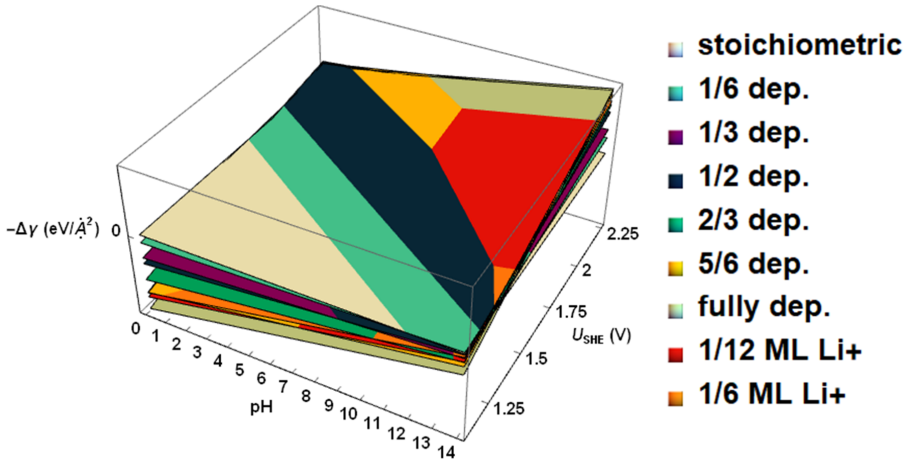

Figure 2: An example for phase diagram of deprotonation and cation adsorption at NiOOH(0001). Thermodynamic activity of 0.1 was assumed for Li^+.

and Li^+ adsorption. In thermal equilibrium, the most stable deprotonated surface is determined from the lowest $\Delta\gamma^{deprotonation}$ at a given potential and pH. As will be discussed, this way, the Pourbaix diagram for surface deprotonation can be constructed.

Double-layer effects. Cation adsorption/desorption on metallic or oxide surfaces induces a relatively large dipole moment at the interface [42, 43, 44], which interacts with the interfacial electric field caused by the electrode potential. Since the electrode potential is not explicitly accounted for in periodic DFT calculations, the Gibbs free energy needs to be corrected for this effect. Following the approach presented by Mills *et al.* for cation adsorption on fcc(111) electrode surfaces [45], Eq. 4 can be rewritten as,

$$\Delta\gamma^{corrected} = \Delta\gamma^{total} + \frac{p^{dipole}_{slab-ads(|water)} - p^{dipole}_{slab(|water)}}{d}(U_{abs} - U_{PZC}), \quad (8)$$

where $p^{dipole}_{slab-ads(|water)}$ is the induced surface dipole at the deprotonated surface with cation adsorption, and $p^{dipole}_{slab|water}$ is that for the stoichiometric NiOOH (0001) surface. In both cases, the slab forms an interface with a water layer. d

is the width of the double layer, i.e., the distance between electrode surface and electrolyte which lies in the range of 2.5 and 3.5 Å; here, we apply the value of d=3 Å consistent with the previous study [45].

The absolute potential scale, U_{abs}, can be shifted to the SHE scale, using the conversion $U_{abs} = U_{SHE} + 4.44$ eV, as recommended by Trasatti [46]. The potential at zero charge, U_{PZC}, is linearly correlated to the electrode work function in the absence of the electrolyte [47]. However, this correlation is empirical and it depends on the degree of orientation of surface water molecules as well as the electron density redistribution at the interface [48]. Mills *et al.* assumed U_{PZC} as zero in their similar investigation [45]. We consider $U_{PZC} = \Phi^0 + const.$ as hyperparameter, with $\Phi^0 = 5.3$ eV as the experimentally measured work function of NiOOH [49], and evaluate a range of values from (-4.5,-3.5) eV for the constant term. This covers a range of (0.8, 1.8) V vs. SHE for U_{PZC}, in which NiOOH was reported to be stable in a pH range of 2 to 14 [50]. A change in the surface dipole moment relative to the stoichiometric surface due to deprotonation and cation adsorption was obtained from the direct correlation with the corresponding work function shift [51],

$$\Delta p^{dipole} = -\frac{\varepsilon_0}{e}\Delta\Phi = -\frac{1}{180.95}\Delta\Phi, \tag{9}$$

where ε_0 and e are vacuum permittivity and elementary charge. The work function is calculated from the difference between the Fermi energy and the value of the one-electron potential in the vacuum region.

3. Results and Discussion

We first discuss the effect of accounting for explicit water layers as well as the induced dipole on the stable surface structure of NiOOH(0001), followed by the discussion on the origin of this effect. Fig. 3(a) shows the change in the surface Gibbs free energy of adsorption, calculated in the gas phase, as a function of potential for a varying degree of deprotonation (Eq. 4) at a constant pH value of 13. At a given potential, the lowest value of $\Delta\gamma$ corresponds to the most

stable surface state. As the potential increases, deprotonation becomes more favourable at NiOOH(0001). Fig. 3(b) shows the results computed in the gas phase but by accounting for the interaction term of induced surface dipole by deprotonation with the electrode potential (Eq. 8). It is seen that the surface dipole can significantly facilitate the deprotonation by decreasing the free energy of adsorption. This effect will be discussed later by computing $\Delta\Phi$ as a function of the degree of deprotonation.

Figure 3(c) shows the effect of explicit surficial water layers on the stable interface structure of NiOOH(0001)/water for varying degrees of deprotonation. Compared with the gas phase system in Fig. 3(a), surface water molecules tend to prevent deprotonation by increasing the change in the adsorption free energy. In fact, water molecules stabilize surface OH species by forming hydrogen bonds with them. This effect has been explained in more detail in our previous work on the structure of water at NiOOH(0001) [23]. Fig. 3(d) shows the computed phase diagram by accounting for the shift in work function due to both deprotonation and the presence of surface water molecules. As for the discussion on Fig. 3(b), the induced dipole decreases the change in the free energy of adsorption and thereby facilitates deprotonation at a given potential.

Table 3 reports the computed work function and the resulting shift in the surface dipole, both in gas phase and in the presence of explicit water molecules, for varying deprotonation states. Consistent with the recent DFT calculations in Ref. [17] it was found that deprotonation leads to electron transfer from surface Ni atoms to surface O atoms, which is evidenced by the change in the oxidation state of Ni from Ni^{3+} to Ni^{4+}. This leads to a significantly polarized surface as the deprotonation degree increases, and as a result the surface dipole, with a direction towards the surface, increases. It should also be noted that a favourable H-down orientation of water at the surface further increases Δp toward the surface, which is consistent with the previous study [52]. Moreover, our calculated work function of 5.33 eV in the presence of water for the stoichiometric NiOOH surface agrees well with the value reported in an experimental study [49]. In the case of cation adsorption, as reported in Table 3, the electron transfer is from

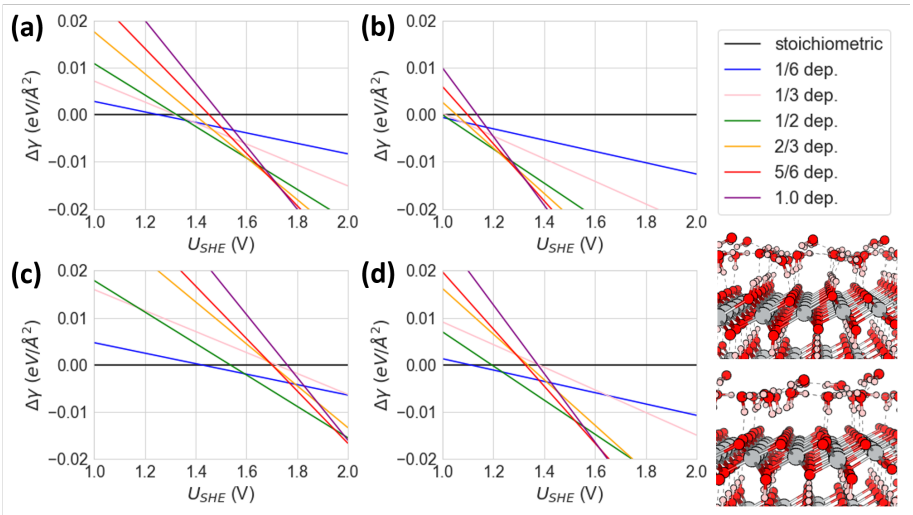

Figure 3: Phase diagram for deprotonation at pH=13. (a) in gas phase, (b) in gas phase with dipole correction, (c) with explicit water layer and (d) with explicit water layer and dipole correction

the adsorbed cation to the surface Ni, resulting in a change in the oxidation state from Ni^{4+} to Ni^{3+}.

Figure 4 shows the shift in work function with respect to the stoichiometric NiOOH(0001) surface as a function of deprotonation and alkali metal cation adsorption. In gas phase calculations, the work function of NiOOH(0001) increases by $\approx$ 3 eV in going from the stoichiometric to the fully deprotonated surface. On the other hand, $\Delta\Phi$ descreases significantly upon cation adsorption in the gas phase, with a visible trend that the larger the cation the more significant the decrease. For the deprotonation process, H-down surface water molecules further contribute to the shift in $\Delta\Phi$, while for cation adsorption strong interactions between water molecules and the cation lead to directional water adsorption and modify the charge distribution at the interface. This results in a smaller drop in the work function for cation adsorption in the presence of water molecules, although the trend with respect to the cation size remains the same as in the gas phase.

To understand the cation size effect on the electronic charge distribution, we

Table 3: Calculated work function and induced surface dipole for various surface adsorption states along with the oxidation state of surface Ni atoms.

adsorption state	Work Function (eV)	Surface Dipole (D)	Oxidation State
stoichiometric | gas (water)	4.96 (5.33*)	0.0 (-0.00987)	12 Ni^{3+}
1/6 deprotonated | gas (water)	5.43 (5.93)	-0.01254 (-0.0258)	1 Ni^{4+}, 11 Ni^{3+}
1/3 deprotonated | gas (water)	5.91 (6.44)	-0.02523 (-0.03934)	2 Ni^{4+}, 10 Ni^{3+}
1/2 deprotonated | gas (water)	6.47 (6.91)	-0.04009 (-0.05181)	3 Ni^{4+}, 9 Ni^{3+}
2/3 deprotonated | gas (water)	7.03 (7.52)	-0.05501 (-0.068)	4 Ni^{4+}, 8 Ni^{3+}
5/6 deprotonated | gas (water)	7.63 (7.80)	-0.07081 (-0.07544)	5 Ni^{4+}, 7 Ni^{3+}
1.0 deprotonated | gas (water)	8.21 (8.10)	-0.08632 (-0.0834)	6 Ni^{4+}, 6 Ni^{3+}
1.0 dep. – 1/12 Li* | gas (water)	6.80 (7.49)	-0.04891 (-0.06709)	5 Ni^{4+}, 7 $Ni4^{3+}$
1.0 dep. – 1/12 Na* | gas (water)	6.03 (7.36)	-0.02845 (-0.06379)	5 Ni^{4+}, 7 Ni^{3+}
1.0 dep. – 1/12 K* | gas (water)	5.17 (7.10)	-0.00571 (-0.05693)	5 Ni^{4+},7 Ni^{3+}
1.0 dep. – 1/12 Cs* | gas (water)	4.98 (6.95)	-0.00067 (-0.05287)	5 Ni^{4+}, 7 Ni^{3+}

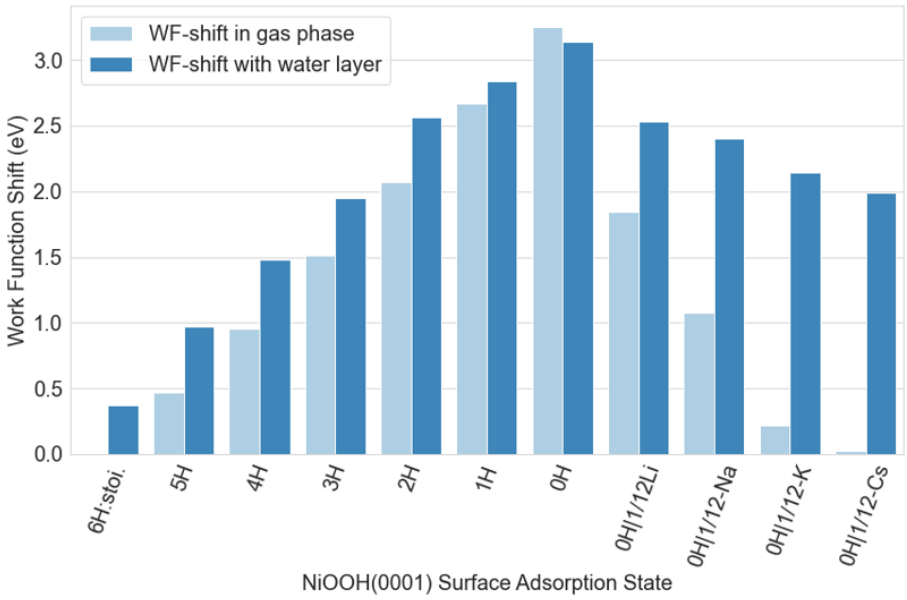

Figure 4: Shift in the work function relative to the stoichiometric NiOOH(0001) surface in the gas phase for varying deprotonation degree and adsorption of alkaline metal cations, in the absence and presence of explicit surface water molecules.

analyzed the charge density difference caused by electron transfer between the various adsorbed cations and the NiOOH(0001) surface in the gas phase. Figure (a) shows the XY averaged charge density difference along the surface normal from which the internal charge polarization can be observed by the adsorption of larger cations, i.e., K^+ and Cs^+. This effect can be better illustrated by showing the 3D charge density difference, as presented in Fig. (b). Unlike Li^+ and Na^+, electronic charge e^- is accumulated on K^+ and Cs^+. As shown in Fig. (c), the internal charge polarization for larger cations leads to a significant potential drop along the surface normal and thereby a larger decrease in $\Delta\Phi$. This shows that not only purely ionic effects play a role upon the specific adsorption of ions on electrode surfaces. With the consideration of explicit water molecules, this effect is suppressed due to the strong interaction of water with adsorbed cations and the resulting charge redistribution. Interestingly enough, such a strong reduction of the work function due to a stronger polarization of larger adsorbed ions has also been observed for anionic halide adsorption on metal surfaces [51, 53].

The effect of alkali metal cation adsorption on the electronic structure of metals and oxides has been a lasting subject of interest [42, 43, 44]. Lindgren and Wallden reported the work function change of Cu(111) upon varying the coverage of Na^+ and Cs^+ [54]. Similar trends were observed for both cations including (1) a coverage-dependent change in the work function, (2) a significant drop of around 2-4 eV at lower coverage, (3) a minimum in the curve at lower coverage. Moreover, the decrease was found to be larger for Cs^+ than Na^+. In addition, the same trend was reported for K^+/Rh(111) [55], Cs^+/W(100) [56], and for Na^+, K^+, Cs^+ adsorption on TiO_2(100) [57]. A more recent experimental study reported that the local work function around an adsorbed K^+ decreases by 1.5 ± 0.3 eV on CuO thin films. Realizing this local effect is particularly important for oxide surfaces where adsorbed alkali metals invoke more localized charge transfer as compared with the metal surfaces [58].

Figure 6 shows the computed Pourbaix diagrams of NiOOH(0001) considering different degrees of deprotonation and also Li^+ adsorption. In the absence of

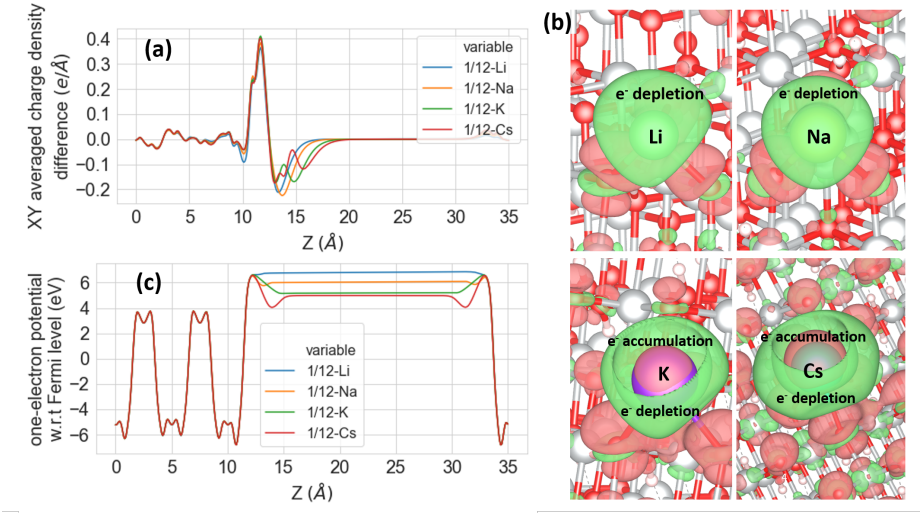

Figure 5: (a) In plane (XY) averaged charge density difference, (b) 3D charge density difference. Green shows electron depletion zone, purple shows electron accumulation zones. (c) XY averaged one-electron potential along the surface normal for various alkali metal cation adsorption at NiOOH(0001)

explicit surface water molecules, as depicted in Figure 6(a), deprotonation becomes more favourable as the pH and potential increase; however, in this case Li^+ adsorption is less favorable than deprotonation, thus its corresponding surface state does not appear in the diagram. This is mainly due to the large negative standard redox potential of alkali metals, which shifts $\Delta\gamma$ of the corresponding surface state to more positive values (see Eq. 4, Eq. 7, Table 2 and Figure 2). To balance this effect, one needs to further stabilize the cations on the surface. Figure 6(b) shows the Pourbaix diagram generated from gas phase calculations but accounting for the dipole interaction term in the surface free energy of adsorption (Eq. 8). As previously discussed, the interaction of the induced dipole moment, that is caused by deprotonation, with the electrode potential further facilitates the deprotonation at lower potentials and lower pH values; however, still with this correction Li^+ adsorbed state is less favorable than deprotonation states which is in contradiction with experiment [16].

Given the relatively large experimental Li^+ solvation free energy of -4.985 eV [45,

59], it is crucial to include solvation effects for the adsorbed cations. As shown in Fig. 6(c) for the system at 5/6 ML water coverage, the strong interaction between water molecules and Li^+, as well the hydrogen bond formation between water and the surface, lead to further stabilization of the interface structure and appearance of Li^+ adsorption in the high potential and pH region of the Pourbaix diagram. Thus, there is a competitive adsorption between Li^+ and protons, similar to the competitive adsorption between chloride and protons on Pt(111) [60, 61, 62].

As shown in Fig. 6(d), including the dipole effects caused by both surface water and deprotonation significantly modified the computed Pourbaix diagram and shifted the stable regions to lower potential and pH values. In other words, the interaction of induced dipole with electrode potential facilitates both deprotonation and Li desorption from the surface. Figure S1 illustrates the sensitivity of the generated Pourbaix diagrams to the hyperparameters of the model, namely, the potential of zero charge and the width of the double layer.

The computed Pourbaix diagrams for the adsorption of other alkali metal cations are shown in Figure S2. Whereas we also find a stability pocket for Na^+ adsorption, no stable K^+ and Cs^+ adsorbate phases appear in the calculated Pourbaix diagrams. This is due to the fact that the larger the cations, the more positive the shift in their Gibbs free energy of adsorption. K^+ and Cs^+ might still adsorb on NiOOH(0001), but at lower concentrations which are associated with a smaller mutual dipole-dipole repulsion upon adsorption. Unfortunately, such low concentrations are below the scope of the present study because of the significantly increased computational effort for larger surface unit cell required to model lower concentrations. Another possibility would be that K^+ and Cs^+ are present as non-specifically adsorbed cations.

The substantial difference between the Pourbaix diagrams in Fig. 6(a) and Figure 6(d) indicates the importance of accounting explicitly for the surficial water layer and dipole interaction effects to obtain an accurate prediction of the stable interface structure for these systems. In this respect, oxide and hydroxide electrodes also behave differently compared to close-packed metal electrodes. For

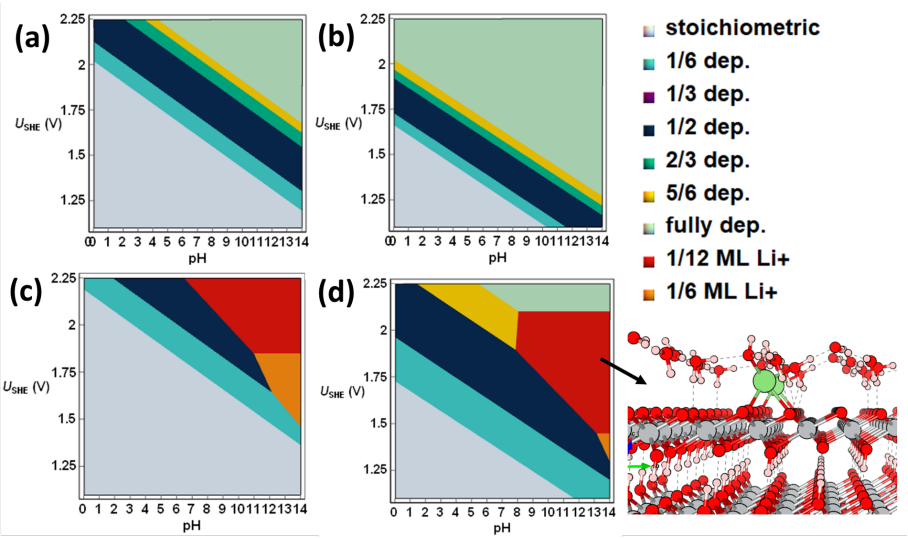

Figure 6: Computed Pourbaix diagram for deprotonation and Li adsorption at NiOOH(0001) in (a) gas phase, (b) gas phase with dipole correction (c) with explicit water layer, (d) with explicit water layer and accounting for dipole correction. A thermodynamic activity of 0.1 was assumed for Li^+.

example, in the grand-canonical evaluation of the Pourbaix diagrams of Pt(111) in contact with halide-containing aqueous electrolytes the explicit and also implicit presence of water can be safely neglected, still a semi-quantitative agreement with the experiment can be obtained [62]. This is due to the relatively weak and rather non-directional interaction of liquid water with close-packed metal electrodes [63]. In contrast, the interaction of water with hydroxide and oxide surfaces has a much stronger covalent character leading to a much more directional bonding of the water molecules, which then becomes significantly modified in the presence of adsorbed cations.

This study represents the first important step towards a better understanding of the enhancement in the OER activity due to surface deprotonation and alkali metal cation adsorption on NiOOH. We speculate that this enhancement is linked with the stronger polarizability of the cations that increases with their size and thereby also leads to larger decrease in the work function upon specific adsorption. Experimental strategies have been proposed to enhance the OER

activity of NiOOH-based materials by manipulating the work function through electron injection [64], which would support our speculation. However, we did not find stable specific adsorbate phases for the two largest cations K^+ and Cs^+ under operating conditions. Hence this change of the work function might also be caused by non-specifically adsorbed cations. Furthermore, it remains to be seen whether the direct interaction of the adsorbed alkali metal cations with the reaction intermediates of the OER also contributes to the enhancement. Further DFT-based computations are required to understand this effect.

4. Conclusions

In order to elucidate the role of the presence of alkali ions for the activity of the oxygen evolution reaction, we applied a grand-canonical scheme based on the computational hydrogen electrode to determine the most stable interface structures of β-NiOOH/water under varying pH and electrode potential for the deprotonation and alkali metal cation adsorption processes. We discussed the crucial importance of double-layer effects due to induced surface dipole moment and the explicit treatment of surficial water molecules. We found that the surface electronic properties change significantly with the size of the adsorbed cations due to their stronger polarizability. This indicates that not only purely ionic effects occur upon the adsorption of ions on electrode surfaces. Accounting for these effects provided an explanation on the experimentally observed alkali metal cation adsorption on the deprotonated NiOOH surfaces under OER conditions. Still, open questions remain with respect to the particular form of the cation adsorption phases which will be the focus of ongoing research efforts.

5. Acknowledgement

Financial support by the Alexander-von-Humboldt Foundation is gratefully acknowledged. This work contributes to the research performed at CELEST (Center for Electrochemical Energy Storage Ulm-Karlsruhe).

References

[1] S. Fujimori, X. Su, J.-Y. Liu, T. Hasegawa, K. Takahashi, T. Masui, M. Takimi, Implication of Paris agreement in the context of long-term climate mitigation goals, SpringerPlus 5 (2016) 1–11.

[2] A. Campen, K. Mondal, T. Wiltowski, Separation of hydrogen from syngas using a regenerative system, Int. J. Hydrogen Energ. 33 (1) (2008) 332–339.

[3] W. T. Hong, M. Risch, K. A. Stoerzinger, A. Grimaud, J. Suntivich, Y. Shao-Horn, Toward the rational design of non-precious transition metal oxides for oxygen electrocatalysis, Energy Environ. Sci. 8 (5) (2015) 1404–1427.

[4] H. A. Miller, K. Bouzek, J. Hnat, S. Loos, C. I. Bernäcker, T. Weißgärber, L. Röntzsch, J. Meier-Haack, Green hydrogen from anion exchange membrane water electrolysis: a review of recent developments in critical materials and operating conditions, Sustain. Energy Fuels 4 (5) (2020) 2114–2133.

[5] M. J. Eslamibidgoli, J. Huang, T. Kadyk, A. Malek, M. Eikerling, How theory and simulation can drive fuel cell electrocatalysis, Nano Energy 29 (2016) 334–361.

[6] S. D. Ebbesen, S. H. Jensen, A. Hauch, M. B. Mogensen, High temperature electrolysis in alkaline cells, solid proton conducting cells, and solid oxide cells, Chem. Rev. 114 (21) (2014) 10697–10734.

[7] M. Gong, W. Zhou, M.-C. Tsai, J. Zhou, M. Guan, M.-C. Lin, B. Zhang, Y. Hu, D.-Y. Wang, J. Yang, et al., Nanoscale nickel oxide/nickel heterostructures for active hydrogen evolution electrocatalysis, Nat. Commun. 5 (1) (2014) 1–6.

[8] M. David, C. Ocampo-Martínez, R. Sánchez-Peña, Advances in alkaline water electrolyzers: A review, J. Energy Storage 23 (2019) 392–403.

[9] L. Trotochaud, S. L. Young, J. K. Ranney, S. W. Boettcher, Nickel–iron oxyhydroxide oxygen-evolution electrocatalysts: the role of intentional and incidental iron incorporation, J. Am. Chem. Soc. 136 (18) (2014) 6744–6753.

[10] D. Friebel, M. W. Louie, M. Bajdich, K. E. Sanwald, Y. Cai, A. M. Wise, M.-J. Cheng, D. Sokaras, T.-C. Weng, R. Alonso-Mori, et al., Identification of highly active Fe sites in (Ni, Fe) OOH for electrocatalytic water splitting, J. Am. Chem. Soc. 137 (3) (2015) 1305–1313.

[11] A. K. Taylor, I. Andreu, B. D. Gates, Regular dimpled nickel surfaces for improved efficiency of the oxygen evolution reaction, ACS Appl. Energy Mater. 1 (4) (2018) 1771–1782.

[12] M. T. Paul, B. B. Yee, D. R. Bruce, B. D. Gates, Hexagonal arrays of cylindrical nickel microstructures for improved oxygen evolution reaction, ACS Appl. Mater. Interfaces 9 (8) (2017) 7036–7043.

[13] R. P. Lamsal, M. S. Houache, A. Williams, E. Baranova, G. Jerkiewicz, D. Beauchemin, Single particle inductively coupled plasma mass spectrometry with and without flow injection for the characterization of nickel nanoparticles, Anal. Chim. Acta 1120 (2020) 67–74.

[14] J. van Drunen, B. Kinkead, M. C. Wang, E. Sourty, B. D. Gates, G. Jerkiewicz, Comprehensive structural, surface-chemical and electrochemical characterization of nickel-based metallic foams, ACS Appl. Mater. Interfaces 5 (14) (2013) 6712–6722.

[15] O. Diaz-Morales, D. Ferrus-Suspedra, M. T. Koper, The importance of nickel oxyhydroxide deprotonation on its activity towards electrochemical water oxidation, Chem. Sci. 7 (4) (2016) 2639–2645.

[16] A. C. Garcia, T. Touzalin, C. Nieuwland, N. Perini, M. T. Koper, Enhancement of oxygen evolution activity of nickel oxyhydroxide by electrolyte alkali cations, Angew. Chem. Int. Ed. 58 (37) (2019) 12999–13003.

[17] A. Govind Rajan, J. M. P. Martirez, E. A. Carter, Facet-independent oxygen evolution activity of pure β-NiOOH: different chemistries leading to similar overpotentials, J. Am. Chem. Soc. 142 (7) (2020) 3600–3612.

[18] M. Li, S. Sakong, A. Groß, In search of the active sites for the selective catalytic reduction on tungsten-doped vanadia monolayer catalysts supported by TiO_2, ACS Catal. 11 (2021) 7411–7421. doi:https://doi.org/10.26434/chemrxiv.14363567.v1.

[19] J. Huang, A. Malek, J. Zhang, M. H. Eikerling, Non-monotonic surface charging behavior of platinum: a paradigm change, J. Phys. Chem. C 120 (25) (2016) 13587–13595.

[20] J. Huang, T. Zhou, J. Zhang, M. Eikerling, Double layer of platinum electrodes: Non-monotonic surface charging phenomena and negative double layer capacitance, J. Chem. Phys. 148 (4) (2018) 044704.

[21] M. J. Eslamibidgoli, M. H. Eikerling, Approaching the self-consistency challenge of electrocatalysis with theory and computation, Curr. Opin. Electrochem. 9 (2018) 189–197.

[22] M. J. Eslamibidgoli, M. H. Eikerling, Atomistic mechanism of Pt extraction at oxidized surfaces: insights from DFT, Electrocatalysis 7 (4) (2016) 345–354.

[23] M. J. Eslamibidgoli, A. Groß, M. Eikerling, Surface configuration and wettability of nickel (oxy) hydroxides: A first-principles investigation, Phys. Chem. Chem. Phys. 19 (34) (2017) 22659–22669.

[24] J. M. P. Martirez, E. A. Carter, Effects of the aqueous environment on the stability and chemistry of β-niooh surfaces, Chem. Mater. 30 (15) (2018) 5205–5219.

[25] A. Van der Ven, D. Morgan, Y. Meng, G. Ceder, Phase stability of nickel hydroxides and oxyhydroxides, J. Electrochem. Soc. 153 (2) (2005) A210.

[26] P. Oliva, J. Leonardi, J. Laurent, C. Delmas, J. Braconnier, M. Figlarz, F. Fievet, A. d. Guibert, Review of the structure and the electrochemistry of nickel hydroxides and oxy-hydroxides, J. Power Sources 8 (2) (1982) 229–255.

[27] G. Kresse, J. Furthmüller, Efficient iterative schemes for ab initio total-energy calculations using a plane-wave basis set, Phys. Rev. B 54 (16) (1996) 11169.

[28] G. Kresse, J. Furthmüller, Efficiency of ab-initio total energy calculations for metals and semiconductors using a plane-wave basis set, Comput. Mater. Sci. 6 (1) (1996) 15–50.

[29] P. E. Blöchl, Projector augmented-wave method, Phys. Rev. B 50 (24) (1994) 17953.

[30] J. P. Perdew, K. Burke, M. Ernzerhof, Generalized gradient approximation made simple, Phys. Rev. Lett. 77 (18) (1996) 3865.

[31] S. Dudarev, G. Botton, S. Savrasov, C. Humphreys, A. Sutton, Electron-energy-loss spectra and the structural stability of nickel oxide: An LSDA+U study, Phys. Rev. B 57 (3) (1998) 1505.

[32] Y.-F. Li, A. Selloni, Mechanism and activity of water oxidation on selected surfaces of pure and Fe-doped NiO_x, ACS Catal. 4 (4) (2014) 1148–1153.

[33] M. Cococcioni, S. De Gironcoli, Linear response approach to the calculation of the effective interaction parameters in the LDA+U method, Phys. Rev. B 71 (3) (2005) 035105.

[34] H. J. Monkhorst, J. D. Pack, Special points for brillouin-zone integrations, Phys. Rev. B 13 (12) (1976) 5188.

[35] J. K. Nørskov, J. Rossmeisl, A. Logadottir, L. Lindqvist, J. R. Kitchin, T. Bligaard, H. Jonsson, Origin of the overpotential for oxygen reduction at a fuel-cell cathode, J. Phys. Chem. B 108 (46) (2004) 17886–17892.

[36] A. A. Peterson, F. Abild-Pedersen, F. Studt, J. Rossmeisl, J. K. Nørskov, How copper catalyzes the electroreduction of carbon dioxide into hydrocarbon fuels, Energy Environ. Sci. 3 (9) (2010) 1311–1315.

[37] A. Groß, S. Sakong, Modelling the electric double layer at electrode/electrolyte interfaces, Curr. Opin. Electrochem. 14 (2019) 1–6.

[38] A. Groß, Grand-canonical approaches to understand structures and processes at electrochemical interfaces from an atomistic perspective, Curr. Opin. Electrochem. 27 (2021) 100684.

[39] J. K. Nørskov, T. Bligaard, A. Logadottir, J. Kitchin, J. G. Chen, S. Pandelov, U. Stimming, Trends in the exchange current for hydrogen evolution, J. Electrochem. Soc. 152 (3) (2005) J23.

[40] F. Gossenberger, T. Roman, A. Groß, Equilibrium coverage of halides on metal electrodes, Surf. Sci. 631 (2015) 17–22.

[41] F. Gossenberger, F. Juarez, A. Groß, Sulfate, bisulfate, and hydrogen coadsorption on Pt(111) and Au(111) in an electrochemical environment, Front. Chem. 8 (2020) 634.

[42] H. P. Bonzel, Alkali-metal-affected adsorption of molecules on metal surfaces, Surf. Sci. Rep. 8 (2) (1988) 43–125.

[43] T. Aruga, Y. Murata, Alkali-metal adsorption on metals, Prog. Surf. Sci. 31 (1-2) (1989) 61–130.

[44] R. D. Diehl, R. McGrath, Structural studies of alkali metal adsorption and coadsorption on metal surfaces, Surf. Sci. Rep. 23 (2-5) (1996) 43–171.

[45] J. Mills, I. McCrum, M. Janik, Alkali cation specific adsorption onto fcc (111) transition metal electrodes, Phys. Chem. Chem. Phys. 16 (27) (2014) 13699–13707.

[46] S. Trasatti, et al., The absolute electrode potential: an explanatory note (recommendations 1986), Pure Appl. Chem 58 (7) (1986) 955–966.

[47] S. Trasatti, Work function, electronegativity, and electrochemical behaviour of metals: II. potentials of zero charge and "electrochemical" work functions, J. Electroanal. Chem. Interf. Electrochem. 33 (2) (1971) 351–378.

[48] J. Le, M. Iannuzzi, A. Cuesta, J. Cheng, Determining potentials of zero charge of metal electrodes versus the standard hydrogen electrode from density-functional-theory-based molecular dynamics, Phys. Rev. Lett. 119 (1) (2017) 016801.

[49] E. L. Ratcliff, J. Meyer, K. X. Steirer, A. Garcia, J. J. Berry, D. S. Ginley, D. C. Olson, A. Kahn, N. R. Armstrong, Evidence for near-surface NiOOH species in solution-processed NiO_x selective interlayer materials: impact on energetics and the performance of polymer bulk heterojunction photovoltaics, Chem. Mater. 23 (22) (2011) 4988–5000.

[50] L.-F. Huang, M. Hutchison, R. Santucci Jr, J. R. Scully, J. M. Rondinelli, Improved electrochemical phase diagrams from theory and experiment: the Ni–water system and its complex compounds, J. Phys. Chem. C 121 (18) (2017) 9782–9789.

[51] F. Gossenberger, T. Roman, K. Forster-Tonigold, A. Groß, Change of the work function of platinum electrodes induced by halide adsorption, Beilstein J. Nanotechnol. 5 (1) (2014) 152–161.

[52] S. Schnur, A. Groß, Properties of metal–water interfaces studied from first principles, New J. Phys. 11 (12) (2009) 125003.

[53] T. Roman, F. Gossenberger, K. Forster-Tonigold, A. Groß, Halide adsorption on close-packed metal electrodes, Phys. Chem. Chem. Phys. 16 (27) (2014) 13630–13634.

[54] S. Lindgren, L. Wallden, Electronic structure of clean and oxygen-exposed Na and Cs monolayers on Cu(111), Phys. Rev. B 22 (12) (1980) 5967.

[55] G. Castro, H. Busse, U. Schneider, T. Janssens, K. Wandelt, Geometric and electronic structure of potassium on Rh(111), Phys. Scr. 1992 (T41) (1992) 208.

[56] C. Papageorgopoulos, J. Chen, Coadsorption of electropositive and electronegative elements: I. Cs and H_2 on W(100), Surf. Sci. 39 (2) (1973) 283–312.

[57] S. Y. Davydov, I. Noskov, Effect of adsorption of alkali metal atoms on the work function of rutile, Tech. Phys. 47 (11) (2002) 1481–1483.

[58] Z. Peng, B. Di, W. Li, D. Liu, X. Wen, H. Zhu, H. Song, Y. Zhang, C. Yin, X. Zhou, et al., Reversibly switching the charge state and adsorption location of a single potassium atom on ultrathin CuO films, Angew. Chem. Int. Ed. 59 (34) (2020) 14321–14325.

[59] Y. Marcus, Ion properties, CRC Press, 1997.

[60] N. Garcia-Araez, V. Climent, E. Herrero, J. Feliu, J. Lipkowski, Thermodynamic studies of chloride adsorption at the Pt(111) electrode surface from 0.1 M $HClO_4$ solution, J. Electroanal. Chem. 576 (1) (2005) 33–41.

[61] N. Garcia-Araez, V. Climent, E. Herrero, J. M. Feliu, J. Lipkowski, Determination of the Gibbs excess of H adsorbed at a Pt(111) electrode surface in the presence of co-adsorbed chloride, J. Electroanal. Chem. 582 (1-2) (2005) 76–84.

[62] F. Gossenberger, T. Roman, A. Groß, Hydrogen and halide co-adsorption on Pt(111) in an electrochemical environment: a computational perspective, Electrochim. Acta 216 (2016) 152–159.

[63] S. Sakong, A. Groß, Water structures on a Pt (111) electrode from ab initio molecular dynamic simulations for a variety of electrochemical conditions, Phys. Chem. Chem. Phys. 22 (19) (2020) 10431–10437.

[64] X. Wang, X. Liu, C.-J. Tong, X. Yuan, W. Dong, T. Lin, L.-M. Liu, F. Huang, An electron injection promoted highly efficient electrocatalyst of FeNi 3@ GR@ Fe-NiOOH for oxygen evolution and rechargeable metal–air batteries, J. Mater. Chem. A 4 (20) (2016) 7762–7771.